Article:

Khan, M., Churnetski, K., Barlow, D. E.M. et al. (2026) Performance enhancement of direct-drive shock-augmented ignition inertial fusion implosions through shock timing optimization. Physical Review E. 065210. ISSN: 1550-2376

https://doi.org/10.1103/zl4y-4blx

Performance enhancement of direct-drive shock-augmented ignition inertial fusion implosions through shock timing optimization

M. Khan,[1,2,*] K. Churnetski,[3] D. E. M. Barlow,[4,5] R. Betti,[3] C. Freeman,[1,2] K. Glize,[1] J. Kunimune,[6] A. Lees,[3] R. Mancini,[7] A. Nutter,[1,2] R. W. Paddock,[1] S. Regan,[3] C. Stoeckl,[3] W. Theobald,[3,8] N. Woolsey,[2] and R. H. H. Scott[1]

[1]*Central Laser Facility, STFC Rutherford Appleton Laboratory, Harwell Campus, United Kingdom*
[2]*York Plasma Institute, School of Physics, Engineering and Technology, University of York, York, United Kingdom*
[3]*Laboratory for Laser Energetics, University of Rochester, Rochester, New York, USA*
[4]*CEA, DAM, DIF, Arpajon, France*
[5]*LULI, École Polytechnique, F-91128 Palaiseau, France*
[6]*MIT PSFC, Cambridge, Massachusetts, USA*
[7]*Department of Physics, University of Nevada, Reno, Nevada, USA*
[8]*Focused Energy GmbH, Im Tiefen See 45, Darmstadt, Germany*

(Received 19 June 2025; revised 16 February 2026; accepted 15 May 2026; published 16 June 2026)

Shock-augmented ignition (SAI) [R. H. H. Scott *et al.*, Phys. Rev. Lett. **129**, 195001 (2022)] is an alternative inertial confinement fusion concept that is designed to achieve high energy gain by combining improved resilience to instabilities with enhanced fuel compression. In SAI, lower implosion velocities can improve hydrodynamic stability and limited laser intensities reduce the excitation of detrimental laser-plasma instabilities, enabling greater areal density accumulation. Here we report an experimental investigation of SAI using a series of warm D_2 implosions. By timing the augmenting shock to arrive at the implosion center immediately prior to peak compression, the areal density and hot-spot pressure increase by 50% and 112%, respectively, relative to unoptimized designs. Ignition-scale simulations reproduce the observed timing dependence and demonstrate the potential of SAI for inertial fusion energy.

DOI: 10.1103/zl4y-4blx

I. INTRODUCTION

The direct-drive approach to inertial confinement fusion (ICF) [1] illuminates a spherical capsule of fusion fuel directly with quasispherically arranged lasers. The capsule has an outer shell of low-*Z* material, typically CH, containing a layer of frozen deuterium-tritium (DT) ice and a core of DT gas. The absorption of laser energy by the outer CH layer causes it to ablate away and, through the conservation of momentum, the remaining target accelerates inwards. Spherical convergence and compression via shocks that are launched by increases in laser intensity raise the gas core temperature and pressure, and a central "hot spot" is formed. This high pressure hot spot resists the further influx of the fuel shell and converts the capsule's kinetic energy into internal energy. For a hot spot with sufficient temperature, $\gtrsim 5$ keV, and areal density, $\rho R \gtrsim 0.3$ g/cm^2, the hot spot ignites and a burn wave propagates through the compressed fuel [1]. Demonstrating the ability to assemble and ignite such fusion plasmas provides the potential for low-carbon, baseload power plants. With the achievement of ignition at the National Ignition Facility (NIF) [2,3] and the proximity to hydro-equivalent direct-drive ignition [4,5], focus now turns to identifying robust high gain designs that are relevant to inertial fusion energy [6].

Shock-augmented ignition (SAI) [7] is a novel scheme that aims to exploit the hydrodynamic stability and high areal density fuel accumulation of low velocity implosions, where ignition is triggered with an augmenting shock; a late-timed shock wave launched without the need for high laser intensities. In conventional implosion designs [1], ignition is achieved through the kinetic energy of the shell alone, necessitating high implosion velocities. This causes susceptibility to hydrodynamic instabilities that can inject ablator material into the DT fuel [8], and mix cold fuel with the hot spot that quenches ignition [9]. Shock ignition (SI) [10] is an alternative design that reduces the implosion velocity and compensates by supplementing the internal energy with a late-timed shock wave. This shock triggers ignition for an already assembled, but subignition, hot spot. The promise of this scheme is that implosions are predicted to be more hydrodynamically stable and allow a greater mass of fuel to be assembled for the same laser energy. However, launching the igniting shock requires a sudden increase, or "spike," in laser intensity to values far beyond thresholds for laser-plasma instabilities (LPI). LPI direct laser energy away from ablation and compression [11], and

*Contact author: matthew.khan@stfc.ac.uk

cause the production of potentially detrimental suprathermal hot electrons [12]. SAI offers the opportunity to realize the benefits of SI with a lower exposure to LPI, as well as the possibility for higher energy gains compared with conventional implosion designs. These higher gains are predicted to be more achievable due to the increased stability.

This article introduces direct-drive shock-augmented ignition implosion experiments. We demonstrate experimentally that key implosion performance metrics can be significantly enhanced by optimizing the SAI laser pulse shape. This improvement in performance is attributed to the impact of the augmenting shock wave and the precise tuning of its launch time. The innovative SAI laser pulse shape features a fall and rise in laser intensity, which allows for a controlled drop in plasma pressure that facilitates the launch of a shock wave in an extended ablation plasma. This occurs at substantially lower laser intensities compared to shock ignition. The shock launch timings yielding the greatest implosion performance improvement are found to align with simulated predictions, which replicate the trends in key implosion metrics inferred from experiment.

The central design features of SAI is a reduction in laser intensity after the main compression drive which preconditions the ablation plasma, followed by a rapid increase in laser intensity to launch a late-timed shock wave. A substantially reduced laser intensity of 1.3×10^{15} W/cm^2 is required compared with $\sim 1 \times 10^{16}$ W/cm^2 for SI [7]. This plasma preconditioning aids the shock launching through a slight relaxation of the ablation plasma, lowering the electron and then ion temperature through electron-ion equilibration. This lowers both the ion-acoustic speed and the local pressure [13], reducing the threshold needed to form a shock. The augmenting shock is subsequently launched in this preconditioned plasma by a rapid rise in laser power. The strength of the shock increases as it spherically converges on the capsule center. After colliding with the return shock from the main compression drive within the in-flight shell, it is designed to supplement the hot-spot internal energy and trigger ignition.

Implosion designs that incorporate a dip and rise similar to SAI are currently in use on OMEGA for high performing shots [14]. Though not used for shock formation, these features are implemented to reduce the growth of Rayleigh-Taylor instabilities due to the larger density scale lengths and increased in-flight aspect ratio from a slightly decompressed shell—benefits also captured by the dip in SAI implosions. The dip depth and rise height provide additional parameters for optimizing implosions, significantly increasing the design space and effectively bridging the gap between these high performance shots and conventional SI. A generative AI model [15] has predicted that, compared with SI, SAI has a wider parameter space for producing high gains, which would make it more appropriate for implementing in power plants. Simulations [16] that use a nonlocal model for the heat conduction predict an increase in the shock launching capabilities over simulations that only use a flux limiter. These models, which are expected to be more accurate, suggest that the requirements for the laser temporal shaping can be reduced, lowering laser complexity and offering the potential for higher gain.

Plasma preconditioning, alternatively referred to as decompression-recompression [17], is anticipated to have significant utility beyond direct-drive SAI. It has been proposed for use in indirect drive, where greater areal density can be achieved while limiting hydrodynamic instability growth [7,18,19]. Simulations have suggested that introducing a dip and spike in the x-ray radiation temperature to marginally subigniting implosions can nearly triple the gain, while also lowering the implosion velocity and improving the stability of the ice-ablator interface [7]. There is ongoing research into the use of heavy-ion beams as efficient drivers for SAI, where substantial improvements in gain are predicted for optimally timed shock launches [20]. Plasma preconditioning is also predicted to aid in shock-induced fuel assembly for the fast ignition implosion scheme [21].

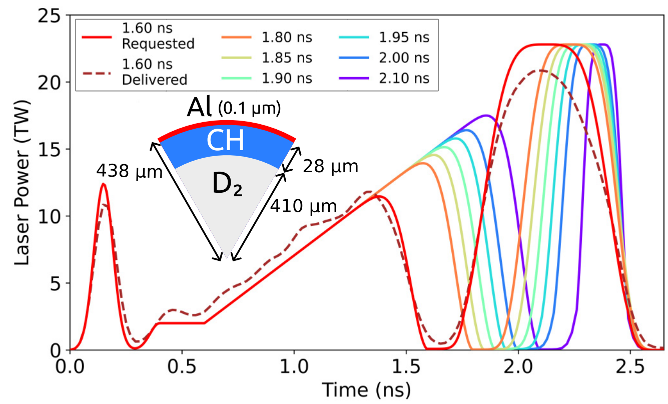

FIG. 1. Equal energy laser pulse designs (∼21 kJ) for dip times of 1.6–2.1 ns given in the legend. Each uses an identical picket, foot, and ramp gradient. Overlaid on the 1.6-ns dip time design is the delivered laser pulse. Also shown is a schematic of the target design. An 876-μm outer diameter capsule, with a 28-μm-thick plastic shell, coated with 100 nm of aluminum, and a deuterium gas fill.

II. EXPERIMENTAL SETUP

The experiment presented here was carried out at the OMEGA Laser Facility at the Laboratory for Laser Energetics [22]. The near-spherically arranged 60 beams illuminated capsules, whose design is depicted in Fig. 1. Various beam smoothing techniques were utilized, including maximum bandwidth SSD [23], SG5-850 phase plates [24], polarization smoothing [25], and distributed polarization rotators [26]. These room temperature capsules had a thin 100-nm outer coating of Al, an outer diameter of ∼876 μm, an ∼28-μm-thick 1.04-g/cm^3 plastic shell, and a deuterium gas-filled core at ∼18 atm.

The laser pulse designs are also shown in Fig. 1 where each used an equivalent ∼21 kJ of laser energy. The pulses begin with an identical picket and foot at 150 and 400 ps, respectively, followed by the main compressive drive with a constant gradient power rise. The late-time dip in laser power and subsequent rise is progressed from 1.6 to 2.1 ns, spanning the simulated optimal timing window. The duration of the shock launching spike was extended for the earlier dip-timed shots in order to maintain energy equivalence across all pulse shapes. An example delivered laser pulse is also shown where, despite the decrease in spike energy, simulations indicate that strong shocks were still launched across all delivered pulses.

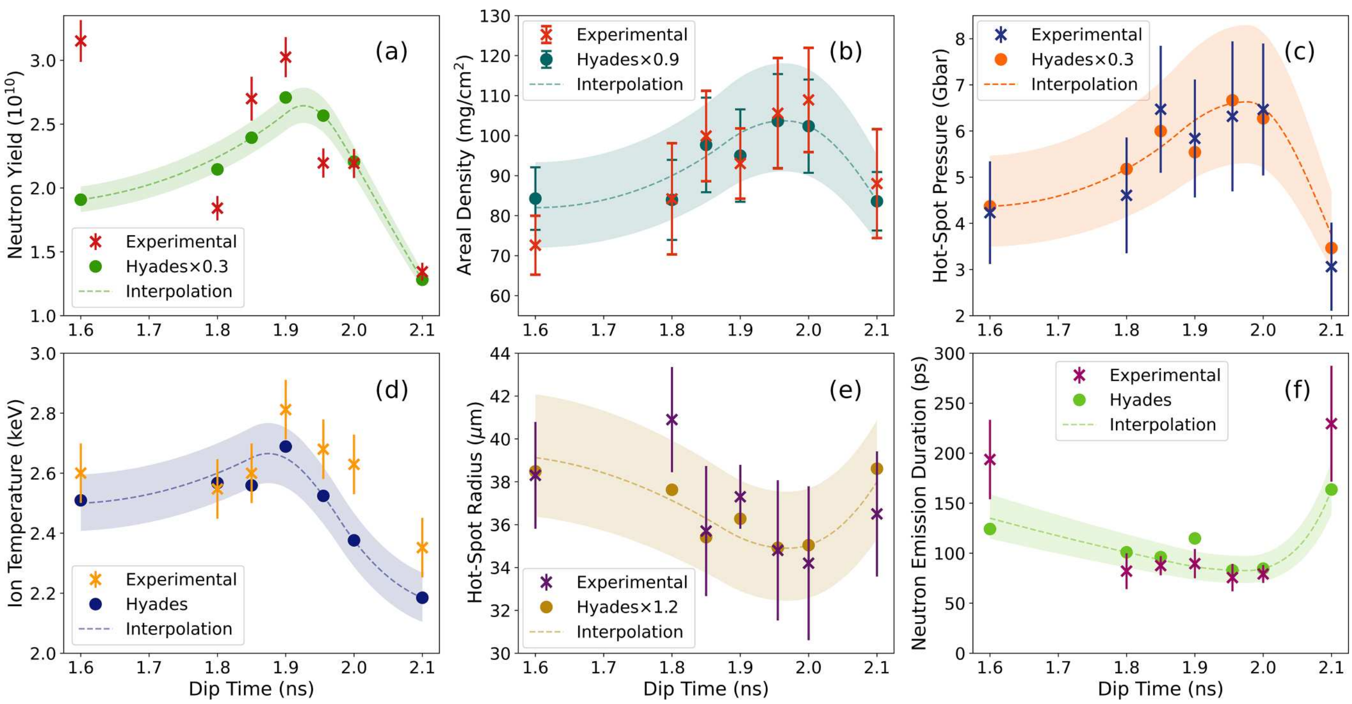

FIG. 2. Implosion performance metrics against dip time (common x axis), shown with scaled simulated values. Ion temperature and areal density are neutron-averaged values, and the hot-spot radius is the 17% contour. The dashed lines are a spline interpolation of the simulation data points to guide the eye and do not represent actual simulation results. The shaded region indicates values that lie within the mean experimental uncertainty of the interpolation line.

Neutron time of flight diagnostics [27] were used to measure the total neutron yield and neutron-averaged hot-spot ion temperature [28]. Areal density was determined from wedge range filter (WRF) diagnostics [29] by the downscatter of secondary protons. The neutron emission rate and bang time (peak emission) were recorded by the neutron temporal diagnostic (NTD) [30]. The hot-spot radius was estimated from a self-emission profile, recorded by the SLOS-TRXI (single line-of-sight time-resolved x-ray imager) diagnostic [31,32].

III. IMPLOSION PERFORMANCE METRICS

At subignition scales, the overall performance of an inertial fusion implosion cannot be described by one single metric. In this work, we are evaluating performance based on three key metrics: neutron yield, areal density, and hot-spot pressure. An implosion will be considered high performing if it attains high values across all three parameters, where one cannot be degraded in favor of maximizing another. This is because to underachieve in one metric would inherently limit the overall performance of an implosion when scaled to an ignition platform.

In the design of the experiment, emphasis was placed upon demonstrating a clear overall performance increase when optimizing the SAI pulse shape, rather than maximizing a single metric such as yield. Further performance, including yield, may be gained from optimizing the compression drive, target specifications, and dip and spike characteristics. According to simulations, a key benefit of SAI is the increase in areal density at stagnation which results in the overall yield enhancement being most effectively seen for implosions at or near ignition scale. On a subignition platform such as this, the efficacy of the scheme can be best demonstrated through the relative improvement in overall performance metrics within the experiment.

Figure 2 depicts experimental and simulated values for several key implosion metrics, plotted against the timing of the dip's minimum laser power. The implosion simulations were performed with HYADES, a Lagrangian radiation-hydrodynamics code [33,34]. These one-dimensional (1D) simulations present an idealized model of an implosion that do not fully capture all the mechanisms that can degrade experimental performance metrics compared with simulations. These include, but are not limited to, laser energy coupling to laser-plasma instabilities, as well as higher-dimensional effects such as hydrodynamic instabilities and drive asymmetries. In order to account for this degradation and to improve the ability to compare the predicted and experimental trends, certain simulated values have been multiplied by a scaling factor. This assumes that the degradation mechanisms can be characterized by a single value and are independent of dip timing, the validity of which is discussed later. Though the scaling factors themselves have been applied individually, the mechanisms that cause them are interconnected, and it was found that the relevant scaling factors were largely consistent with the others. It should be noted again that it is the trend in the metrics with respect to dip timing that is most important, rather than the absolute agreement, as this best highlights the ability to model the impact of the timing of the shock launch on an implosion.

The total neutron yield and neutron-averaged hot-spot temperature that are given in Figs. 2(a) and 2(d) are specifically hot-spot metrics since for these noncryogenic targets all fusion reactions occur in the hot spot. A neutron yield-over-clean (YOC) ratio, defined as the ratio of measured to predicted yield, of 0.3 was achieved here. Yield is thought to be strongly degraded by hydrodynamic instabilities, first during the acceleration phase where target defects and laser imprint act as seeds for instability growth [35], and the deceleration phase where cold shell material is mixed with the high-temperature hot spot, lowering the temperature and quenching yield [36].

Areal density is shown in Fig. 2(b) and acts as a proxy for the fuel assembly capabilities. The simulated results have been corrected for the impact of the hot-spot mix that quenches the yield [37,38], the method for which is outlined in Appendix A. Areal density estimates were well aligned with simulations, with a small 10% degradation observed, potentially due to hydrodynamic instabilities during the acceleration phase.

Hot-spot pressure, shown in Fig. 2(c), is an effective measure of the implosion performance as a whole, requiring both a high-temperature hot spot and large areal densities. It can be estimated from measurable implosion characteristics [39], following the method outlined in Appendix B. Equation (B1) in Appendix B predicts that the hot-spot pressure reduces by a factor of 0.41 due to a YOC of 0.3 and a hot-spot radius of 1.2 times larger. An Additional reduction in the experimental hot-spot pressure from 0.41 to 0.3 will arise from other degradation sources.

The hot-spot radius given in Fig. 2(e) is compared against postprocessed simulations using SPECT3D [40] that models the self-emission profile. The hot-spot radii were ∼20% larger than simulations, similar to previous warm plastic shelled implosions [41], and consistent with the reduced compressive piston action from a slightly degraded areal density.

The neutron emission duration is plotted in Fig. 2(f). It is expected that high performing implosions have a narrow emission duration [42], where larger durations can be an indication of poor kinetic to internal energy conversion at stagnation [43].

Across all metrics, a general trend emerges in both the simulated and experimental results. Optimal values occur for dip timings of ∼1.85–2.0 ns, and diminish away from this peak. Shots timed close to this optimum typically achieve the highest values in all key metrics, with exceptions discussed later. The experimental trends are well modeled by the simulations, with deviations away from the scaled values being within experimental uncertainties, suggesting that the degradation mechanisms mentioned above cause systematic decreases. The correlation of the optimal range between the experimental results and the simulations highlights our ability to model the effectiveness of the dip and spike, increasing our confidence in our ability to accurately simulate the scheme as a whole. The relative flatness of the experimental hot-spot pressures within the range of optimal timings suggests that there is a robust high performance window for the timing of the shock launch such that it does not require exceptionally stringent timing requirements.

It can be seen in Fig. 2(b) that the areal density increased by ∼50% when the dip timing was progressed from the early timed 1.6 ns shot to the more optimally timed 2.0 ns shot. When comparing dip times of 2.0 and 2.1 ns in Fig. 2(c), the hot-spot pressure saw a dramatic improvement of $\gtrsim$110%. Despite only a small change in the dip timing, this improvement in hot-spot pressure highlights the effectiveness of the shock and the importance of its timing. According to Fig. 2(a), the yield of the 2.0-ns dip-timed shot saw an increase of 65% compared with the later timed 2.1 ns shot, though a much larger increase of ∼130% was seen for 1.9 ns which, while not the highest performing shot overall, is still firmly within the region of optimal timings.

Despite the high yield of the 1.6-ns dip-timed shot, it is not considered to be high performing given its low areal density and hot-spot pressure. The high yield can be understood by the impact of the earlier timed shock launch. The early shock launch increases the entropy of the capsule earlier in the implosion. The increase in entropy improves the shell's hydrodynamic robustness, making it less susceptible to the higher-dimensional degradations. The implosion then performs closer to the 1D simulation and the yield is elevated compared with the later dip times. The increased entropy, however, limits the areal density that can be reached at peak compression, suggesting that areal density was compromised in favor of yield. Additionally, the neutron emission duration was over twice as large as the more optimally timed 1.9 ns shot and with a 30% lower peak emission rate. These features combined illustrate that, despite the high yield, it was overall a low performance implosion, suggesting that the shock was launched too early for it to provide maximum benefit.

The launch and timing of the augmenting shock are inferred from simulations, constrained by the delivered laser pulses and measured observables, that are then used to interpret the measured performance metrics. The correlation between the experimental trends and the modeled predictions, in the absence of an alternative explanation consistent with the observed timing dependence, strongly suggests the existence of the augmenting shocks. Appendix C provides an assessment of the impact of dominant implosion degradation mechanisms on performance. It is found that, for all mechanisms considered, the magnitude of degradation was either minimal or showed no correlation with dip timing. This implies that, consistent with both pre- and postshot simulations, the variation in the augmenting shock timing is the causal factor behind the observed performance trends.

With the exceptions to the performance trends noted above, the agreement between the simulated and experimental results, combined with the elimination of alternative degradation mechanisms, provides justification for the use of the single-valued scalings. This suggests that these assumed degradations are systematic and independent of shock launch timing.

IV. TEMPORAL REMAPPING OF SHOCK LAUNCHING

Upon interrogation of the simulated shock dynamics, the time at which the shock arrives at the hot-spot center with respect to the compressive yield was found to be a central factor in determining its performance benefit. The augmenting shock must be timed such that it arrives at the hot-spot center immediately preceding the peak in yield generated through compression alone. At ignition scales, the supplementary internal

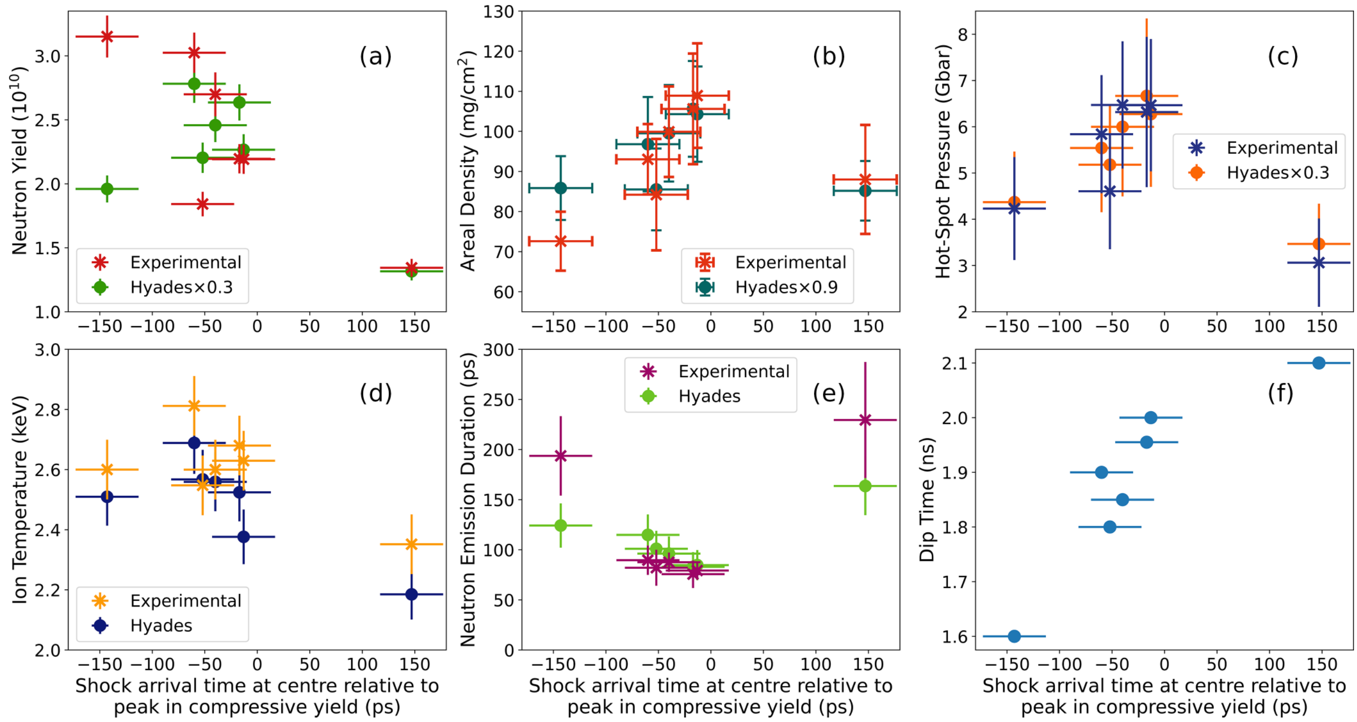

FIG. 3. Implosion performance metrics, as shown in Fig. 2, against the predicted arrival time of the augmenting shock at capsule center with respect to the time of the peak in compressive yield (common x axis). The mapping of dip timing to shock arrival time is given in plot (f).

energy increase due to the shock pushes the hot spot beyond the threshold where α bootstrapping will initiate ignition. Shocks that arrive too early will require much higher strengths and with greater energies to ignite due to the limited hot-spot areal density at that early time. For shocks that arrive after the peak in compressive yield, the energy loss from capsule disassembly that immediately follows peak compression is greater than the supplementary shock energy, and no benefit is gained.

Figures 3(a)–3(e) show the same metrics as shown in Fig. 2 where the timings now reflect the predictions of the shock arrival time at the hot-spot center relative to the peak in the compressive yield, such that positive values represent the shock arriving late. The mapping of the dip timing to the shock arrival time is given in Fig. 3(f). This shock arrival time must be extracted from simulations and thus uncertainties associated with simulation accuracy must be applied. The same trends in performance metrics largely reemerge with this new timing where the optimal range occurs near shock co-timing with compressive yield. The trends in yield and ion temperature are less defined, though still somewhat apparent, with both peaking at ~0–50 ps before being co-timed. The areal density appears to reach its peak values at or just before co-timing, though it is acknowledged that the late-time shock region is not extensively explored by these experiments. The larger neutron emission durations of the 1.6- and 2.1-ns dip-timed shots shown in Fig. 2(f) can now be understood as the result of the compressive yield duration being extended by a mistimed shock-induced yield.

HYADES is able to model the bang time of these implosions with a mean accuracy of ~75 ps and standard deviation of ~30 ps. However, bang time is an absolute measurement and this temporal reordering tracks the relative timing of two features. As such, it is expected that the uncertainty for the retiming will likely be less than the uncertainty in the bang-time estimation, and differences will largely be systematic. The timing uncertainty given in Fig. 3 is 30 ps to reflect the standard deviation of bang-time differences. The inherent minor deviations of the delivered laser pulse compared with the requested design, as seen in Fig. 1, have impacted the even distribution of shock arrival times.

V. IGNITION-SCALE SIMULATIONS

Ignition-scale SAI implosion simulations were performed using the capsule and laser design outlined in [7]. Reproduced here are the neutron yields for implosions where the power of the dip was reduced to zero, and the timing of the dip and spike were scanned. The capsules had a 3502 μm outer diameter, with a 51-μm CH ablator and a 165-μm DT ice fuel layer, and a total laser energy of 1.9 MJ. The shock arrival time at the implosion center was similarly extracted from simulations.

These ignition scale simulations highlight the potential capabilities of the SAI scheme and further emphasize the importance of shock timing. Figure 4 depicts (a) the fusion energy output against shock launching time and (b) against shock arrival time with respect to the α-off compressive yield. or something similar, wanting to indicate which is figure (a) and (b). The high yields of >100 MJ that are predicted are of strong relevance to inertial fusion energy. The ignition window for launching the shock, defined as the time interval where 80% of the maximum yield is achieved, is ~500 ps, similar to SI window durations [44] and importantly within the capabilities of contemporary laser systems.

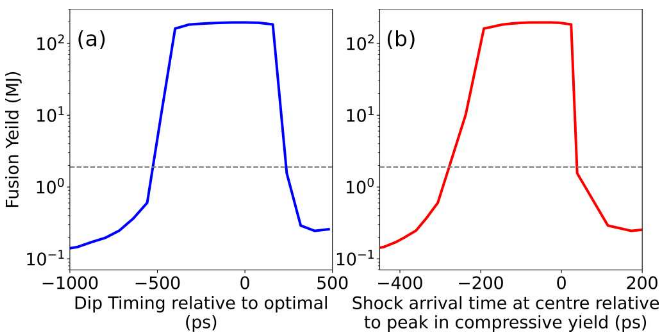

FIG. 4. Simulations of direct-drive SAI implosions using 1.9 MJ of laser energy. Fusion energy yield against (a) dip timing with respect to the optimal value and (b) arrival time of the augmenting shock relative to the peak in the α-off compressive yield. The dashed gray line represents (a) the input laser energy and (b) a gain of 1.

Figure 4(b) effectively illustrates that the timing of the shock arrival is essential for optimizing implosion designs. A gentle rise in yield is seen for early arrival time shocks ($\gtrsim$200 ps before peak compression), as seen in SI [44]. Here, the shock simply adds to the conventional implosion mechanism and so provides little benefit, similar to the experimental 1.6-ns dip-timed shot. For timings of between ~200 ps before peak compression and co-timed arrival, the shock is able to provide the necessary energy at the correct time and triggers ignition, with the peak in yield occurring at ~30 ps before the shock is co-timed with peak compression. This corresponds with the best performing window of 1.8–2.0-ns dip-timed shots. For shock arrival later than peak compression, there is insufficient time to ignite the hot spot before the capsule disassembles and ignition fails, similar to the 2.1-ns dip-timed shot.

Much of the SI literature discusses the importance of the igniting shock colliding with the return shock near the inner edge of the compressed fuel [10]. The sharp cutoff of yield at ~0 ps seen in Fig. 4(b) illustrates that the timing of the shock arrival at the implosion's center with respect to peak compression must also be considered alongside the location of the shock collision as an essential aspect of implosion design. A similar reasoning has been provided for determining the location of an SI ignition cliff [44].

A limiting factor in the scaling of SI implosions to ignition scale is the uncertainty in the impact of LPI for laser-plasma conditions predicted for a larger energy platform. SAI is unlikely to be impacted as strongly as SI at ignition scales due to the reduced laser intensity, therefore there can be greater confidence in the correspondence of subscale implosions such as those presented here, with the high gain predicted in ignition scale simulations. Furthermore, realizing SI with current laser capabilities would require separate beams to supply the compressive drive and the high intensity spike due to power delivery limitations [45]. Since SAI can launch the igniting shock with significantly reduced intensities, these additional beams are not needed, which may decrease the cost of a power plant.

VI. CONCLUSIONS

To conclude, we have conducted direct-drive shock-augmented ignition implosions. It has been shown that optimally timing the launch of the augmenting shock provides a clear performance improvement whose range aligns with simulated predictions. SAI uses a lower implosion velocity than conventional implosion designs and a lower intensity than SI, reducing hydrodynamic and laser-plasma instabilities, respectively. These results establish SAI as a promising route to improved implosion stability and higher gains, with the potential to expand the viable parameter space, providing a compelling pathway towards the realization of inertial fusion energy.

ACKNOWLEDGMENTS

The authors thank the staff of the Target Diagnostics and Target Area Operations teams at the OMEGA Laser Facility. We gratefully acknowledge the funding from EPSRC Grants No. EP/P023460/1, No. EP/P026796/1, and EP/L01663X/1.

This work was funded in part by the UK's Department for Energy Security and Net Zero as part of UPLiFT, the "UK Programme of Laser Inertial Fusion Technology for Energy."

This material is based upon work supported in part by the Department of Energy (National Nuclear Security Administration), University of Rochester "National Inertial Confinement Fusion Program" under Award No. DE-NA0004144.

This report was prepared as an account of work sponsored in part by an agency of the U.S. Government. Neither the U.S. Government nor any agency thereof, nor any of their employees, makes any warranty, express or implied, for the accuracy, completeness, or usefulness of any information, apparatus, product, or process disclosed, or represents that its use would not infringe privately owned rights. Reference herein to any specific commercial product, process, or service by trade name, trademark, manufacturer, or otherwise does not necessarily constitute or imply its endorsement, recommendation, or favoring by the U.S. Government or any agency thereof. The views and opinions of the authors expressed herein do not necessarily state or reflect those of the U.S. Government or any agency thereof.

DATA AVAILABILITY

The data that support the findings of this article are openly available [46].

APPENDIX A: SIMULATED AREAL DENSITY CORRECTION

Secondary protons produced through the D(d, p)T reaction escape the hot spot and are collected by WRF diagnostics. As they travel through and collide with the compressed shell material, they downscatter in energy and the amount of energy loss can then be used to calculate the shell areal density. Proton production is closely matched with the neutron production rate from the primary D(d, n)He reactions [47] which is recorded with the NTD detectors. The resulting areal density is a "neutron-averaged" value, which is to say an averaging over the neutron production history, as calculated by Eq. (A1).

$$\langle \rho R \rangle_{\text{simulated}} = \frac{\int n_{\text{rate}}^{\text{sim}}(t) \times \rho R^{\text{sim}}(t) \mathrm{d}t}{\int n_{\text{rate}}^{\text{sim}}(t) \mathrm{d}t}. \tag{A1}$$

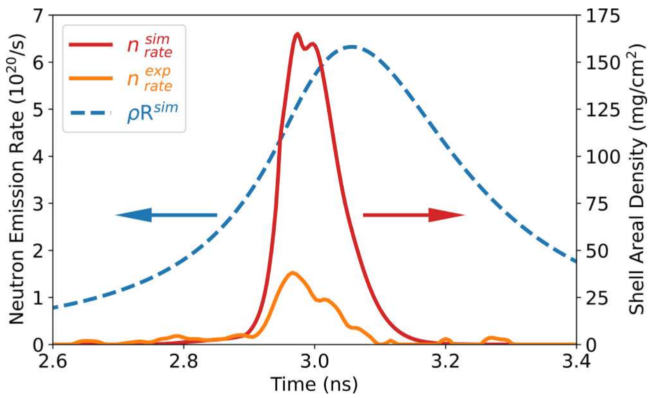

FIG. 5. Experimental and simulated neutron emission rates, with the simulated shell areal density. The areal density peaks later in time compared with the neutron emission rate. The experimental neutron emission is quenched by mixing the shell material into the hot spot due to deceleration phase hydrodynamic instabilities.

Here, $\langle \rho R\rangle_{\text{simulated}}$ is the simulated neutron-averaged areal density and $n_{\text{rate}}^{\text{sim}}$ is the simulated neutron emission rate.

Figure 5 depicts the simulated and experimental neutron emission rates close to stagnation, along with the simulated shell areal density. It can be seen that the peak in areal density occurs slightly later in time than that of the neutron emission rate. Even without any areal density specific degradation mechanisms, experimental areal densities are typically lower than simulations would predict. This is in part due to experimental fusion rates peaking even earlier than in simulations, resulting in a probing of the areal density earlier when it is comparatively lower. This earlier, and indeed lower, peak in neutron rate is thought to be due to deceleration phase hydrodynamic instability that mixes shell material into the hot spot and quenches fusion reactions.

Hydrodynamic instabilities can be seeded on the inner surface of the shell due to surface roughness or feedthrough from additional instabilities on the outside of the shell. During the deceleration phase where the low density hot spot resists the influx of the high density shell, these instabilities grow and lead to mixing of cold and high-Z shell material into the hot spot, quenching fusion reactions and truncating the emission profile in time [37,41]. This can readily be seen from the close alignment of the leading edges of the neutron emission rate and the rapid curtailment of the peak rate and an eventual complete quenching of reactions.

In order to compensate for this, the experimental neutron production rate can be used in place of the simulated rate, along with the simulated areal density. By averaging over the experimental rate, the protons are predicted to travel through a lower, but still idealized, areal density and result in a lower and more relevant predicted value. This corrected value is calculated with Eq. (A2).

$$\langle \rho R\rangle_{\text{corrected}} = \frac{\int n_{\text{rate}}^{\text{expt}}(t) \times \rho R^{\text{sim}}(t)\text{d}t}{\int n_{\text{rate}}^{\text{expt}}(t)\text{d}t}. \tag{A2}$$

Now, $\langle \rho R\rangle_{\text{corrected}}$ is the corrected neutron-averaged areal density prediction, based on the simulated areal density, ρR^{sim}, and the experiment neutron emission rate, $n_{\text{rate}}^{\text{expt}}$.

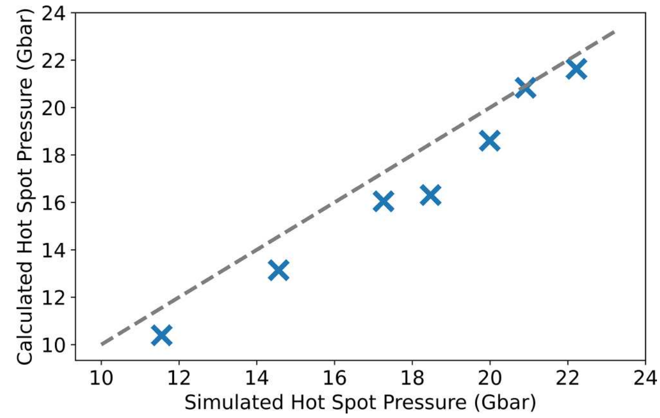

FIG. 6. A comparison of hot-spot pressures from simulations. The x axis gives the simulated neutron-averaged hot-spot pressure and the y axis gives the calculated hot-spot pressure using Eq. (B1) and the simulated implosion outputs. The dashed line represents a perfect agreement.

This value is highly sensitive to the timing of the neutron emission rate. As such, given the timing uncertainty for the NTD is ∼50 ps, the uncertainty for the predicted values given in Figs. 2(b) and 3(b) are found from $n_{\text{rate}}^{\text{expt}}(t \pm 50\text{ ps})$.

APPENDIX B: HOT-SPOT PRESSURE ESTIMATION

Hot-spot pressure, P_{hs}, estimation was originally derived for use in cryogenic DT implosions [39]. It has been adapted here for warm D_2 implosions, given by Eq. (B1),

$$P_{\text{hs}} \approx \left\{16Y\sqrt{\ln 2/\pi}\Big/\left[\Delta\tau \int_{V_{\text{hs}}} dV(\langle\sigma v\rangle_{\text{DD}}/T^2)\right]\right\}^{1/2}, \tag{B1}$$

where Y is the total neutron yield, and $\Delta\tau$ is the neutron emission duration. The hot-spot volume V_{hs} is assumed to be spherical with a radius $R_{\text{hs}} = 1.06R_{17}$ where the 17% intensity contour radius is used as this best aligns with postprocessed hydrodynamics simulations [39]. The D-D fusion reactivity $\langle\sigma v\rangle_{\text{DD}}$ is given in Ref. [48], where only the neutron-producing D(d, n)He reaction channel is used. The hot-spot ion temperature is given by $T(r) = T_c[1 - (r/R_{\text{hs}})^2(1 - 0.15^{3/2})]^{2/3}$ [49] where T_c is the maximum hot-spot temperature, constrained by the neutron-averaged ion temperature.

Figure 6 shows a comparison between the unscaled simulated hot-spot pressure with that found from Eq. (B1), using the simulated hot-spot characteristics. The estimations are largely consistent with the simulated values, lower by a mean of only ∼7.5%. If applicable to the experimental values, the pressures given above might be underestimations and so the absolute performance of the implosions could be higher.

This model assumes an isobaric hot spot [50], which is largely satisfied in the simulations after the augmenting shock has rebounded within the core multiple times. The applicability, however, of the 17% contour for extracting the hot-spot radius has yet to be fully determined for warm plastic shelled implosions. With these considerations, the uncertainties in the

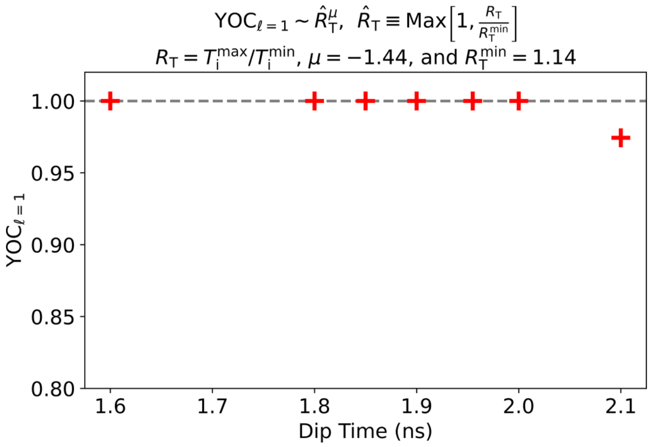

FIG. 7. The neutron yield-over-clean (YOC) degradation predicted for these shots from the mode-1 asymmetries. The magnitude of the asymmetry is judged from the differences in measured ion temperature as viewed along different lines of sight, and the degradation is then calculated by the formula given in the figure title.

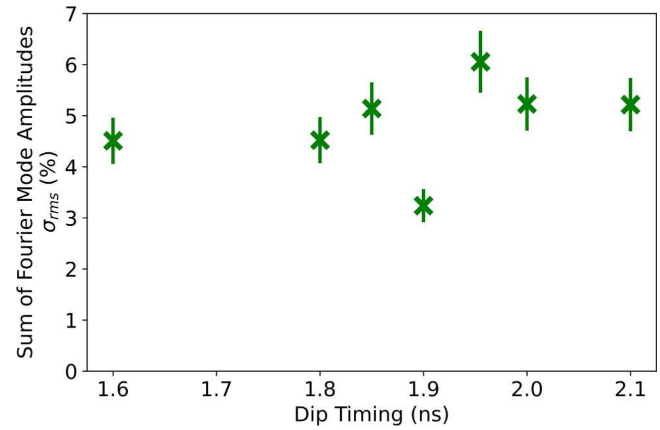

FIG. 8. The sum of the Fourier mode amplitudes for modes 2–10 against dip timing. No consistent relationship is seen between them.

pressures have been increased, and we justify its use here, given that it is a relative performance increase that is being established rather than an absolute measure. These uncertainties are expected to be systematic and so intra-experiment comparisons are most likely valid.

APPENDIX C: ALTERNATIVE DEGRADATION MECHANISMS

In order to eliminate them as potential causes for the trends in the performance metrics, an assessment of alternative degradation mechanisms that are common to ICF implosions were performed; mode-1 asymmetries, low and mid-mode asphericities, laser-plasma instabilities, and hydrodynamic instabilities. This enables the conclusion that the main factor driving the improvement was the timing of the shock launch. It is shown that, out of the degradations investigated, the magnitude of the degradation is either minimal or has no correlation with dip timing. This suggests that these mechanisms are not driving the observed performance trends.

1. Mode-1 Asymmetries

Deviations from perfectly spherical implosions can be characterized by decomposing the shape of the implosion into spherical harmonics, with associated mode numbers. A mode-1 asymmetry is the motion of the implosion center off the initial capsule center and occurs typically by laser or target mispointing. Mode-1 asymmetries reduce the coupling of shell kinetic energy to hot-spot internal energy and can drive bulk hot-spot flow (residual kinetic energy). Reduced coupling lowers yield and inferred hot-spot pressure. This bulk flow results in a Doppler shift in the ion velocities and so can be assessed by the observed ion temperature across different lines of sight. An experimentally inferred fusion yield dependency model [51] produced from an extensive ensemble of cryogenic OMEGA implosions found that ion temperature asymmetries ($T_{ion}^{max}/T_{ion}^{min}$) of greater than 1.14 were needed to produce a statistically significant reduction in yield. Given that cryogenic implosions typically reach higher convergences and are thus more susceptible to hot-spot flow, this cutoff may be even higher for warm implosions. Only the 2.1-ns dip-timed shot produced a ratio marginally beyond the cutoff, as shown in Fig. 7, which would have led to a yield reduction of only 2.5%, according to the statistical model. It can therefore be concluded that mode-1 asymmetries did not significantly impact the trend in experimental yield or hot-spot pressure.

2. Low and MidMode Asphericities

Beyond the mode-1, the low and mid-mode asphericities are defined here as those with mode numbers between 2 and 10. They can be estimated from the hot-spot self-emission profiles. A Fourier transform of a hot-spot emission contour provides the amplitudes of each mode. This aspherical compression reduces the effective compression, lowering peak areal density, broadening the neutron emission duration, and lowering performance.

Figure 8 shows the sum of these Fourier mode amplitudes, with greater values coming from greater asphericities which lead to greater degradation. Minimal difference in these mode

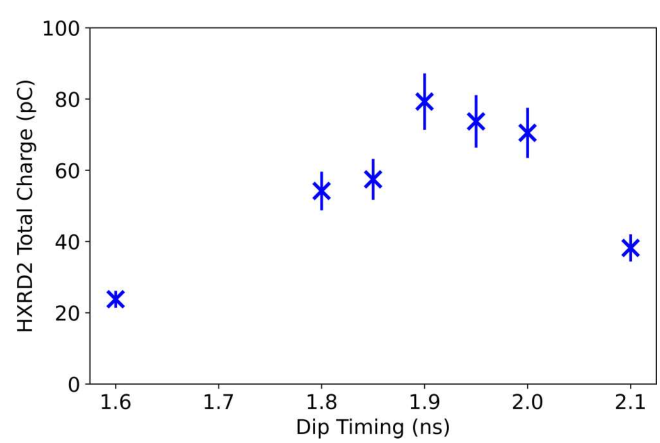

FIG. 9. Charge accumulated in the second channel of the HXRD diagnostic. Greater charge implies a larger population of hot electrons which can preheat the shell and limit peak areal density.

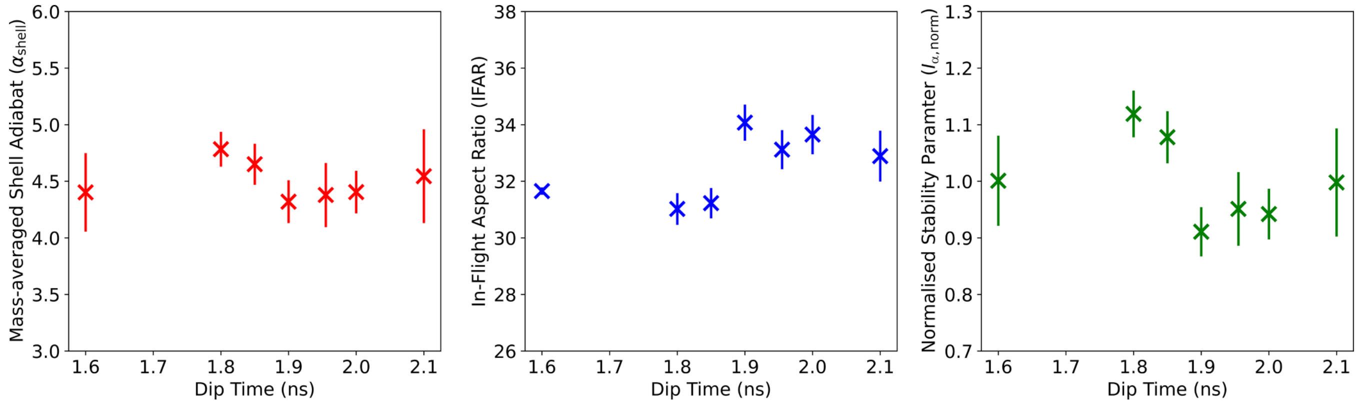

FIG. 10. Key stability metrics against dip timing, evaluated from the postshot simulations at a time of 1.5 ns into the implosion. All metrics show minimal variation with dip timing, as can be expected due to them all having the same requested laser pulse up to this point. Deviations from each other only exist because of the inherent variations in laser pulse delivery. The minimal differences in stability parameter seen here are not expected to significantly change the performance.

amplitudes is seen across the shots, and thus minimal impact is expected on the performance. It should also be noted that the low convergence ratios seen here (< 15) result in less susceptibility to low and mid-modes [51], ruling out the impact of these on performance.

3. Laser-Plasma Instabilities

HXRD [52] is a hard x-ray detector that is sensitive to Bremsstrahlung emission from LPI produced hot electrons that slow down within the shell. These hot electrons can preheat the shell, increase its adiabat and limit peak compression. Higher levels of recorded x-rays indicate greater levels of hot electrons and thus more preheat [53]. Figure 9 shows the relationship between the hot-electron signal (determined from the charge accumulated on channel 2 of the HXRD detector) and dip timing. This suggests that, in fact, the more optimally timed shots were experiencing greater levels of preheat. Not only would the improvement in performance (increase in areal density) not be explained by the hot electron production, if techniques were implemented to reduce hot electron production (high-Z dopants [54], improved laser smoothing [55], increased laser bandwidth [56]), then further improvements in areal density might be seen. It should be noted though, that these hot-electron signals are much weaker than those for typical OMEGA shots [53], meaning their impact, positive or negative, is likely minimal.

We note here that it is currently unclear what role hot electrons will have on the augmenting shock, which may in fact be enhanced by their energy deposition and increase overall performance despite their preheating effect. However, as noted above, a low hot-electron signal was observed for these shots so we can again conclude that they did not significantly impact the performance.

4. Hydrodynamic Stability

The hydrodynamic stability of an imploding capsule is typically judged by the adiabat of the shell, α_{shell}, and the in-flight aspect ratio (IFAR), combined to give a single-valued stability parameter, I_α, as shown in Eq. (C1) [36].

$$I_\alpha \propto \frac{\alpha_{\text{shell}}^{1.1}}{\text{IFAR}}. \tag{C1}$$

High adiabats improve resilience to Rayleigh-Taylor instability growth [57], and low IFARs decrease the penetration of these instabilities through the shell [58], such that high stability parameters result in greater stability. The constant of proportionality has been empirically determined for cryogenic DT shots but is not included here since it has not been verified for warm plastic shelled implosions.

It has been demonstrated experimentally that below a critical value for this parameter, performance is significantly impacted, and that above an additional upper threshold, improvements in the stability parameter do not provide added benefit [59]. It should be noted that there is not one universal method for calculating the IFAR and adiabat—in particular the boundaries for the integration for the mass averaging of the shell adiabat and the time in the implosion where each metric should be judged. Combining this with the added com-

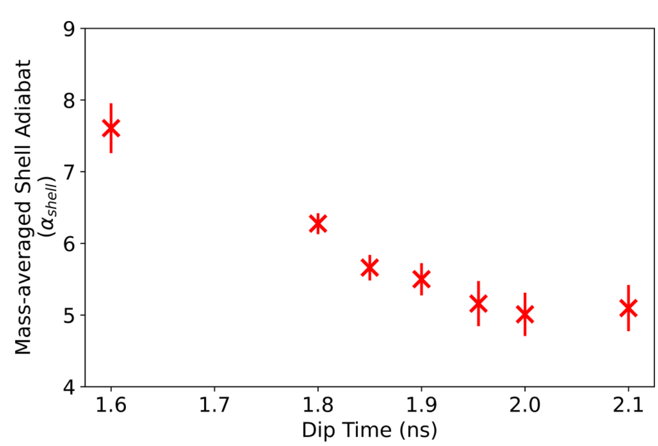

FIG. 11. Mass-averaged shell adiabat against dip timing, evaluated at 2.3 ns when all shocks have been launched and the hot spot is nearing stagnation. The higher adiabats of the earlier timed shots decrease the mixing of the shell within the hot spot but limit peak areal density.

plication of comparing DT cryogenic shots with warm plastic shelled implosions, the absolute values given for the cutoff for stability provided by the statistical model are likely inappropriate for this experiment. Nevertheless, comparing the predicted values from the implosions within this dataset can help identify any outliers in terms of impact on performance. With this in mind and in the absence of a verified constant of proportionality for Eq. (C1), the stability parameter has been normalized to the mean value of all the shots.

Figure 10 shows the adiabat, IFAR, and normalized stability parameter against dip timing, evaluated at $t = 1.5$ ns, chosen to be before any dips in laser power. The variation occurs because of the inherent slight differences in the delivery of the laser pulses. It can be readily seen that, prior to any dips and spikes, they all exhibit very similar stability values.

Figure 11 gives the adiabat when evaluated at $t = 2.3$ ns, after all the shocks have been launched. The larger adiabat of the earlier dip-timed shots can readily be seen. This increased adiabat improves the stability during hot-spot assembly and minimizes the quenching effect discussed earlier. This elevates the YOC, improving the yield relative to the other shots, but will ultimately hold back the overall performance when moving to an igniting platform. The remaining shots are all very similar to each other, indicating that they are experiencing similar levels of hot-spot mix and thus a single-valued scaling (i.e., a single YOC) is most likely appropriate.

[1] R. Craxton, K. Anderson, T. Boehly, V. Goncharov, D. Harding, J. Knauer, R. McCrory, P. McKenty, D. Meyerhofer, J. Myatt, *et al.*, Direct-drive inertial confinement fusion: A review, Phys. Plasmas **22**, 110501 (2015).

[2] H. Abu-Shawareb, R. Acree, P. Adams, J. Adams, B. Addis, R. Aden, P. Adrian, B. Afeyan, M. Aggleton, L. Aghaian, *et al.*, Lawson criterion for ignition exceeded in an inertial fusion experiment, Phys. Rev. Lett. **129**, 075001 (2022).

[3] A. Kritcher, A. Zylstra, C. Weber, O. Hurricane, D. Callahan, D. Clark, L. Divol, D. Hinkel, K. Humbird, O. Jones, *et al.*, Design of the first fusion experiment to achieve target energy gain $G > 1$, Phys. Rev. E **109**, 025204 (2024).

[4] L. Ceurvorst, R. Betti, V. Gopalaswamy, A. Lees, J. Knauer, M. Rosenberg, D. Patel, R. Ejaz, C. Williams, K. Woo, *et al.*, Progress toward hydro-equivalent ignition in OMEGA direct-drive DT-layered implosions, Phys. Plasmas **32**, 032711 (2025).

[5] A. Lees, R. Betti, V. Gopalaswamy, J. Knauer, L. Ceurvorst, D. Patel, R. Ejaz, K. Anderson, K. Bauer, M. Bonino, *et al.*, Approaching hydro-equivalent ignition in laser direct-drive via target design optimization using novel statistical modeling, Phys. Plasmas **32**, 072707 (2025).

[6] X. Ribeyre, H. Chesneau, H. Besaucèle, J. Néauport, and A. Casner, Perspectives in laser-driven inertial fusion reactor system, AIP Adv. **15**, 095013 (2025).

[7] R. H. H. Scott, D. Barlow, W. Trickey, A. Ruocco, K. Glize, L. Antonelli, M. Khan, and N. C. Woolsey, Shock-augmented ignition approach to laser inertial fusion, Phys. Rev. Lett. **129**, 195001 (2022).

[8] C. R. Weber, T. Döppner, D. T. Casey, T. L. Bunn, L. C. Carlson, R. J. Dylla-Spears, B. J. Kozioziemski, A. G. MacPhee, A. Nikroo, H. F. Robey, *et al.*, First measurements of fuel-ablator interface instability growth in inertial confinement fusion implosions on the National Ignition Facility, Phys. Rev. Lett. **117**, 075002 (2016).

[9] S. P. Regan, R. Epstein, B. A. Hammel, L. J. Suter, H. A. Scott, M. A. Barrios, D. K. Bradley, D. A. Callahan, C. Cerjan, G. W. Collins, *et al.*, Hot-spot mix in ignition-scale inertial confinement fusion targets, Phys. Rev. Lett. **111**, 045001 (2013).

[10] R. Betti, C. D. Zhou, K. S. Anderson, J. L. Perkins, W. Theobald, and A. A. Solodov, Shock ignition of thermonuclear fuel with high areal density, Phys. Rev. Lett. **98**, 155001 (2007).

[11] A. Colaïtis, G. Duchateau, X. Ribeyre, Y. Maheut, G. Boutoux, L. Antonelli, P. Nicolaï, D. Batani, and V. Tikhonchuk, Coupled hydrodynamic model for laser-plasma interaction and hot electron generation, Phys. Rev. E **92**, 041101(R) (2015).

[12] R. H. H. Scott, K. Glize, L. Antonelli, M. Khan, W. Theobald, M. Wei, R. Betti, C. Stoeckl, A. G. Seaton, T. D. Arber, *et al.*, Shock ignition laser-plasma interactions in ignition-scale plasmas, Phys. Rev. Lett. **127**, 065001 (2021).

[13] J. D. Huba, *NRL Plasma Formulary* (Naval Research Laboratory, Washington, DC, 1998), Vol. 6790.

[14] C. Williams, R. Betti, V. Gopalaswamy, J. Knauer, C. Forrest, A. Lees, R. Ejaz, P. Farmakis, D. Cao, P. Radha, *et al.*, Demonstration of hot-spot fuel gain exceeding unity in direct-drive inertial confinement fusion implosions, Nat. Phys. **20**, 758 (2024).

[15] M. Ben Tayeb, V. Tikhonchuk, and J.-L. Feugeas, ICF target optimization using generative AI, Phys. Plasmas **31**, 103903 (2024).

[16] W. Q. Yuan, Z. H. Zhao, S. P. Zhu, X. T. He, and B. Qiao, Nonlocal effects on the shock-augmented ignition scheme of laser inertial fusion, Phys. Rev. Res. **6**, 013332 (2024).

[17] L. Wang, W. Ye, J. Wu, J. Liu, W. Zhang, and X. He, A scheme for reducing deceleration-phase Rayleigh-Taylor growth in inertial confinement fusion implosions, Phys. Plasmas **23**, 052713 (2016).

[18] L.-F. Wang, J.-F. Wu, W.-H. Ye, Z.-F. Fan, and X.-T. He, Design of an indirect-drive pulse shape for ∼1.6 MJ inertial confinement fusion ignition capsules, Chin. Phys. Lett. **31**, 045201 (2014).

[19] R. H. H. Scott, R. Nora, A. Zylstra, L. J. Perkins, J. Salmonson, D. D. M. Ho, I. C. Freeman, O. Landen, V. Smalyuk, C. Weber, D. Casey, M. Schneider, W. Trickey, D. E. M. Barlow, and N. C. Woolsey First experiments on the shock-augmented ignition approach to indirect drive laser inertial fusion (unpublished).

[20] S. Nouri, B. Khanbabaei, and S. Khoshbinfar, Shock Augmented ignition target design for heavy ion inertial fusion, Nucl. Instrum. Methods Phys. Res. Sect. A **1088**, 171457 (2026).

[21] H. Nagatomo, T. Johzaki, R. Takizawa, and S. Fujioka, Formation of high areal density core using an efficient and robust implosion method for fast ignition, Nucl. Fusion **64**, 106019 (2024).

[22] T. Boehly, D. Brown, R. Craxton, R. Keck, J. Knauer, J. Kelly, T. Kessler, S. Kumpan, S. Loucks, S. Letzring, *et al.*, Initial performance results of the OMEGA laser system, Opt. Commun. **133**, 495 (1997).

[23] S. Skupsky and R. Craxton, Irradiation uniformity for high-compression laser-fusion experiments, Phys. Plasmas **6**, 2157 (1999).

[24] Y. Kato, K. Mima, N. Miyanaga, S. Arinaga, Y. Kitagawa, M. Nakatsuka, and C. Yamanaka, Random phasing of high-power lasers for uniform target acceleration and plasma-instability suppression, Phys. Rev. Lett. **53**, 1057 (1984).

[25] J. E. Rothenberg, Polarization beam smoothing for inertial confinement fusion, J. Appl. Phys. **87**, 3654 (2000).

[26] T. Boehly, V. Smalyuk, D. Meyerhofer, J. Knauer, D. Bradley, R. Craxton, M. Guardalben, S. Skupsky, and T. Kessler, Reduction of laser imprinting using polarization smoothing on a solid-state fusion laser, J. Appl. Phys. **85**, 3444 (1999).

[27] T. J. Murphy, R. E. Chrien, and K. Klare, Interpretation of neutron time-of-flight signals from current-mode detectors, Rev. Sci. Instrum. **68**, 610 (1997).

[28] C. J. Forrest, P. Radha, V. Y. Glebov, V. Goncharov, J. Knauer, A. Pruyne, M. Romanofsky, T. Sangster, M. Shoup, C. Stoeckl, *et al.*, High-resolution spectroscopy used to measure inertial confinement fusion neutron spectra on Omega (invited), Rev. Sci. Instrum. **83**, 10D919 (2012).

[29] F. Séguin, J. Frenje, C. Li, D. Hicks, S. Kurebayashi, J. Rygg, B.-E. Schwartz, R. Petrasso, S. Roberts, J. Soures, *et al.*, Spectrometry of charged particles from inertial-confinement-fusion plasmas, Rev. Sci. Instrum. **74**, 975 (2003).

[30] C. Stoeckl, R. Boni, F. Ehrne, C. Forrest, V. Y. Glebov, J. Katz, D. Lonobile, J. Magoon, S. P. Regan, M. Shoup, *et al.*, Neutron temporal diagnostic for high-yield deuterium–tritium cryogenic implosions on OMEGA, Rev. Sci. Instrum. **87**, 053501 (2016).

[31] SLOS-TRXI was run here in time-integrated mode.

[32] W. Theobald, C. Sorce, M. Bedzyk, S. Ivancic, F. Marshall, C. Stoeckl, R. Shah, M. Lawrie, S. Regan, T. Sangster, *et al.*, The single-line-of-sight, time-resolved x-ray imager diagnostic on OMEGA, Rev. Sci. Instrum. **89**, 10G117 (2018).

[33] Laser energy was deposited through inverse bremsstrahlung, electron thermal conduction was flux limited ($\alpha = 0.06$), diffusive multigroup radiation and multigroup thermonuclear burn-product transport-energy deposition were employed, and a first-principles equation of state [60] was used. Actual target layer thicknesses and delivered laser power profiles were also used. An empirically derived drive multiplier was used that reproduces Velocity Interferometry System for Any Reflector [61] shock timing data, measured implosion trajectories, and bang times over a wide range of OMEGA direct-drive implosions [62].

[34] J. T. Larsen and S. M. Lane, HYADES—A plasma hydrodynamics code for dense plasma studies, J. Quant. Spectrosc. Radiat. Transfer **51**, 179 (1994).

[35] S. Hu, D. Michel, A. Davis, R. Betti, P. Radha, E. Campbell, D. Froula, and C. Stoeckl, Understanding the effects of laser imprint on plastic-target implosions on OMEGA, Phys. Plasmas **23**, 102701 (2016).

[36] V. N. Goncharov, T. Sangster, R. Betti, T. Boehly, M. Bonino, T. Collins, R. Craxton, J. Delettrez, D. Edgell, R. Epstein, *et al.*, Improving the hot-spot pressure and demonstrating ignition hydrodynamic equivalence in cryogenic deuterium–tritium implosions on OMEGA, Phys. Plasmas **21**, 056315 (2014).

[37] W. Theobald, R. Betti, C. Stoeckl, K. Anderson, J. Delettrez, V. Y. Glebov, V. Goncharov, F. Marshall, D. Maywar, R. McCrory, *et al.*, Initial experiments on the shock-ignition inertial confinement fusion concept, Phys. Plasmas **15**, 056306 (2008).

[38] J. Trela, W. Theobald, K. Anderson, D. Batani, R. Betti, A. Casner, J. Delettrez, J. Frenje, V. Y. Glebov, X. Ribeyre, *et al.*, The control of hot-electron preheat in shock-ignition implosions, Phys. Plasmas **25**, 052707 (2018).

[39] S. Regan, V. Goncharov, I. Igumenshchev, T. Sangster, R. Betti, A. Bose, T. Boehly, M. Bonino, E. Campbell, D. Cao, *et al.*, Demonstration of fuel hot-spot pressure in excess of 50 Gbar for direct-drive, layered deuterium-tritium implosions on OMEGA, Phys. Rev. Lett. **117**, 025001 (2016).

[40] J. MacFarlane, I. Golovkin, P. Wang, P. Woodruff, and N. Pereyra, SPECT3D–A multi-dimensional collisional-radiative code for generating diagnostic signatures based on hydrodynamics and PIC simulation output, High Energy Density Phys. **3**, 181 (2007).

[41] W. L. Shang, C. Stoeckl, R. Betti, S. P. Regan, T. C. Sangster, S. X. Hu, A. Christopherson, V. Gopalaswamy, D. Cao, W. Seka, *et al.*, Properties of hot-spot emission in a warm plastic-shell implosion on the OMEGA laser system, Phys. Rev. E **98**, 033210 (2018).

[42] Y. Arikawa, M. Ota, M. Nakajima, T. Shimizu, S. Segawa, T. N. Khoa Phan, Y. Sakawa, Y. Abe, A. Morace, S. R. Mirfayzi, *et al.*, The conceptual design of 1-ps time resolution neutron detector for fusion reaction history measurement at OMEGA and the National Ignition Facility, Rev. Sci. Instrum. **91**, 063304 (2020).

[43] R. H. H. Scott, D. S. Clark, D. K. Bradley, D. A. Callahan, M. J. Edwards, S. W. Haan, O. S. Jones, B. K. Spears, M. M. Marinak, R. P. J. Town, P. A. Norreys, and L. J. Suter, Numerical modeling of the sensitivity of x-ray driven implosions to low-mode flux asymmetries, Phys. Rev. Lett. **110**, 075001 (2013).

[44] X. Ribeyre, G. Schurtz, M. Lafon, S. Galera, and S. Weber, Shock ignition: An alternative scheme for HiPER, Plasma Phys. Controlled Fusion **51**, 015013 (2009).

[45] W. Theobald, R. Nora, M. Lafon, A. Casner, X. Ribeyre, K. Anderson, R. Betti, J. Delettrez, J. Frenje, V. Y. Glebov, *et al.*, Spherical shock-ignition experiments with the 40 + 20-beam configuration on OMEGA, Phys. Plasmas **19**, 102706 (2012).

[46] M. Khan, K. Churnetski, D. E. M. Barlow, R. Betti, C. Freeman, K. Glize, J. Kunimune, A. Lees, R. Mancini, A. Nutter, R. W. Paddock, S. Regan, C. Stoeckl, W. Theobald, N. Woolsey, and R. H. H. Scott, Dataset for the experiment OMEAGA SAI-23A, 2025, https://edata.stfc.ac.uk/items/e7a22beb-f55a-45a0-a0c7-bca8eb94d849.

[47] J. Frenje, C. Li, J. Rygg, F. Séguin, D. Casey, R. Petrasso, J. Delettrez, V. Y. Glebov, T. Sangster, O. Landen, *et al.*, Diagnosing ablator ρR and ρR asymmetries in capsule implosions using charged-particle spectrometry at the National Ignition Facility, Phys. Plasmas **16**, 022702 (2009).

[48] H.-S. Bosch and G. M. Hale, Improved formulas for fusion cross-sections and thermal reactivities, Nucl. Fusion **32**, 611 (1992).

[49] R. Betti, M. Umansky, V. Lobatchev, V. Goncharov, and R. McCrory, Hot-spot dynamics and deceleration-phase Rayleigh–Taylor instability of imploding inertial confinement fusion capsules, Phys. Plasmas **8**, 5257 (2001).

[50] R. Betti, P. Chang, B. Spears, K. Anderson, J. Edwards, M. Fatenejad, J. Lindl, R. McCrory, R. Nora, and D. Shvarts, Thermonuclear ignition in inertial confinement fusion and comparison with magnetic confinement, Phys. Plasmas **17**, 058102 (2010).

[51] A. Lees, R. Betti, J. P. Knauer, V. Gopalaswamy, D. Patel, K. M. Woo, K. S. Anderson, E. M. Campbell, D. Cao, J. Carroll-Nellenback, *et al.*, Experimentally inferred fusion yield dependencies of OMEGA inertial confinement fusion implosions, Phys. Rev. Lett. **127**, 105001 (2021).

[52] C. Stoeckl, V. Y. Glebov, D. Meyerhofer, W. Seka, B. Yaakobi, R. Town, and J. Zuegel, Hard x-ray detectors for OMEGA and NIF, Rev. Sci. Instrum. **72**, 1197 (2001).

[53] D. Cao, W. Theobald, M. Rosenberg, L. Ceurvorst, D. Patel, A. Christopherson, C. Stoeckl, A. Lees, V. Gopalaswamy, R. Betti, *et al.*, Correlating hot-electron preheat from the two-plasmon decay instability to ρR degradation for direct-drive implosions on OMEGA, Phys. Plasmas **32**, 092708 (2025).

[54] K. Churnetski, D. Patel, W. Theobald, R. Betti, D. Cao, L. Ceurvorst, M. Rosenberg, A. Solodov, C. Stoeckl, and S. Regan, Mitigation of hot-electron preheat from the two-plasmon-decay instability using silicon-doped plastic shells in direct-drive implosions on OMEGA, Phys. Plasmas **31**, 112707 (2024).

[55] D. Turnbull, A. Maximov, D. Cao, A. Christopherson, D. Edgell, R. Follett, V. Gopalaswamy, J. Knauer, J. Palastro, A. Shvydky, *et al.*, Impact of spatiotemporal smoothing on the two-plasmon–decay instability, Phys. Plasmas **27**, 102710 (2020).

[56] D. Froula, C. Dorrer, A. Colaïtis, D. Edgell, R. Follett, E. Hill, I. Igumenshchev, A. Milder, J. Palastro, R. Shah, *et al.*, A future of inertial confinement fusion without laser-plasma instabilities, Phys. Plasmas **32**, 052713 (2025).

[57] J. Knauer, K. Anderson, R. Betti, T. Collins, V. Goncharov, P. McKenty, D. Meyerhofer, P. Radha, S. Regan, T. Sangster, *et al.*, Improved target stability using picket pulses to increase and shape the ablator adiabat, Phys. Plasmas **12**, 056306 (2005).

[58] P. Radha, C. Stoeckl, V. Goncharov, J. Delettrez, D. Edgell, J. Frenje, I. Igumenshchev, J. Knauer, J. Marozas, R. McCrory, *et al.*, Triple-picket warm plastic-shell implosions on OMEGA, Phys. Plasmas **18**, 012705 (2011).

[59] A. Lees, R. Betti, J. P. Knauer, V. Gopalaswamy, D. Patel, K. M. Woo, K. S. Anderson, E. M. Campbell, D. Cao, J. Carroll-Nellenback, *et al.*, Understanding the fusion yield dependencies in OMEGA DT-layered implosion experiments using a physics-based statistical mapping model, Phys. Plasmas **30**, 012709 (2023).

[60] S. X. Hu, B. Militzer, V. N. Goncharov, and S. Skupsky, First-principles equation-of-state table of deuterium for inertial confinement fusion applications, Phys. Rev. B **84**, 224109 (2011).

[61] P. Celliers, G. Collins, L. Da Silva, D. Gold, and R. Cauble, Accurate measurement of laser-driven shock trajectories with velocity interferometry, Appl. Phys. Lett. **73**, 1320 (1998).

[62] M. B. Khan, Advanced direct drive shock ignition studies, Ph.D. thesis, University of York, 2022.